Buoyancy-thermocapillary Convection of Volatile Fluids under their Vapors

Tongran Qin[a], Željko Tuković[b], Roman O. Grigoriev[c]

[a]George W. Woodruff School of Mechanical Engineering, Georgia Institute of Technology, Atlanta, GA 30332-0405, USA
[b]University of Zagreb, Faculty of Mechanical Engineering and Naval Architecture, Ivana Lučića 5, Zagreb, Croatia
[c]School of Physics, Georgia Institute of Technology, Atlanta, GA 30332-0430, USA

Abstract

Convection in a layer of fluid with a free surface due to a combination of thermocapillary stresses and buoyancy has been studied extensively under atmospheric conditions. However, recent experimental results have shown that removing most of the air from a sealed cavity significantly alters the flow structure and, in particular, suppresses transitions between different convection patterns found at atmospheric conditions. On the other hand, removing air has a very small effect on the flow speed, while a simple analytical estimate predicts that complete removal of noncondensable gases such as air should reduce the flow speed by an order of magnitude. To understand these unexpected results, we have formulated and numerically implemented a detailed transport model that takes into account mass and heat transport in both phases in the absence of noncondensables. The model was used to investigate how the flow is affected by the magnitude of the (poorly defined) accommodation coefficient and by the temperature jump across the liquid-vapor interface predicted by some phase change models. Our results eliminate both effects as possible explanations for the unexpected experimental observations, suggesting that the small amount of air left in the cavity in the experiments is the most likely, albeit somewhat unexpected, explanation for the observations.

Keywords: Buoyancy-thermocapillary convection, buoyancy-Marangoni convection, free surface flow, noncondensable gas, thermocapillarity, phase change model, accommodation coefficient

1. Introduction

Convection in liquid films driven by horizontal temperature gradients has attracted attention in the past due to applications to crystal growth in microgravity environments, where evaporation is negligible, buoyancy plays no role, and the flow is driven by thermocapillarity. More recently, the focus shifted to flows driven by a combined action of capillary pressure, thermocapillary forces, and buoyancy with phase change playing an increasingly important role due to applications in thermal management in terrestrial environments. In particular, devices such as heat pipes and heat spreaders, which use phase change to enhance thermal transport, are typically sealed, with noncondensables (such as air), which can impede phase change, removed [1].

The liquid film is almost always in contact with a mixture of its own vapor and air. The fundamental studies on which the design of such devices is based, however, often do not distinguish between different compositions of the gas phase. The experimental studies are typically performed in geometries that are not sealed and hence contain air at atmospheric pressure, while most theoretical studies ignore phase change completely. Those that do consider phase change use transport models of the gas phase that are too crude to properly describe the effect of noncondensables on the flow in the liquid layer. Yet, as a recent experimental study by Li *et al.* [2] shows, noncondensables play an important and nontrivial role, so the results in one limit cannot be simply extrapolated to the other.

We have introduced a proper two-sided model for volatile fluids which provides a detailed description of heat and mass transport in both the liquid and the gas phase dominated by noncondensables in a separate paper [3]. This model, as well as previous experimental studies of volatile and nonvolatile fluids by Villers and Platten [4], De Saedeleer *et al.* [5], Garcimartin *et al.* [6], Riley and Neitzel [7] and Li *et al.* [2], shows that volatile and nonvolatile fluids have similar behavior at atmospheric conditions. At dynamic Bond numbers of order unity, the flow in the liquid layer is relatively fast and transitions from a steady unicellular pattern (featuring one big convection roll) to a steady multicellular pattern (featuring multiple steady convection rolls) to an oscillatory pattern (featuring multiple unsteady convection rolls) as the applied temperature gradient is increased. Numerical studies of nonvolatile fluids by Villers and Platten [4], Ben Hadid and Roux [8], Mundrane and Zebib [9], Lu and Zhuang [10], and Shevtsova *et al.* [11] come to the same basic conclusion, justifying the use of one-sided models in the limit where the gas phase is dominated by noncondensables.

Here our focus is on the opposite limit, where the gas phase is dominated by vapors rather than noncondensables. As the experiments of Li *et al.* [2] conducted for a volatile silicone oil at dynamic Bond numbers $Bo_D \approx 1$ demonstrate, transitions between different convection patterns are suppressed under vapor, and the flow structure remains the same (i.e., qualitatively similar to the unicellular flow under air) when the magnitude of the applied temperature gradient is varied. Moreover, in the vapor-dominated limit, the flow speeds were found to be com-

parable to those in the air-dominated limit, although existing transport models predict that the flow speeds in the absence of noncondensables should decrease substantially.

Proper interpretation of these experimental observation requires fundamental understanding of two-phase flows in confined geometries in the (near) absence of noncondensables, which is currently lacking. There are very few theoretical studies of this limit. Zhang et al. [12] performed an analytical investigation of a model of a sealed rectangular heat-pipe with pure vapor (no air) above an essentially flat liquid layer. Their model, however, was based on a large number of assumptions (Stokes flow, negligible buoyancy, negligible advective fluxes, infinite evaporation and Marangoni numbers) that do not hold for the experimental studies [2]. Kuznetzov and Sitnikov [13] and Kaya and Goldak [14] proposed and numerically investigated models of heat pipes which do not include buoyancy or Marangoni effects, do not conserve mass, and treat the liquid phase in a very restrictive way (as Darcy or lubrication flow). Kafeel and Turan [15] and Fadhl et al. [16] proposed and investigated crude models of thermosyphons which treat the fluid as a mixture of the liquid and vapor phase, with phase change occurring in the bulk rather than at a (non-existing) interface.

To address this deficit, we introduce a comprehensive two-sided model of two-phase flow of a volatile fluid in confined and sealed geometries due to an applied temperature gradient in the absence of noncondensables. This model is described in detail in Section 2. Results of the numerical investigations of this model are presented, analyzed, and compared with experimental findings in Section 3. Finally, Section 4 presents our conclusions.

2. Mathematical Model

2.1. Governing Equations

The vast majority of theoretical studies of buoyancy-thermocapillary convection is based on one-sided models where heat and mass transport in the gas phase are not solved for directly, but rather are incorporated indirectly through boundary conditions at the liquid-vapor interface. As we have shown using a two-sided model [3] which describes heat and mass transport in both phases, Newton's law of cooling, which is the basis of most one-sided models, is generally invalid for convection at atmospheric conditions. Hence, there is no reason, *a priori*, to believe that it should hold in the absence of noncondensables. In order to describe convection in volatile fluids in the absence of noncondensables, the heat and mass transport in both phases must be modeled explicitly.

Zhang *et al.* [12] have previously formulated a two-sided model for the problem considered here in the limit of vanishing Reynolds number and infinite Marangoni and evaporation numbers [17] and and obtained an analytical solution for the case of a pinned contact line and an essentially flat interface. Unfortunately, almost none of these assumptions actually hold in the experiments of Li *et al.* [2], requiring development of a general two-sided model that does not rely on any of these assumptions. Such a model, based on the one described in Ref. [3] is presented below.

Both the liquid and the gas phases can be considered incompressible, since the fluid velocities $\mathbf{u}$ are much smaller than the speed of sound at small length scales. Hence the continuity equation reduces to $\nabla \cdot \mathbf{u} = 0$. Because the fluid velocities can, however, be large enough for inertial effects to be significant, the momentum transport in the bulk should be described by the Navier-Stokes equation

$$\rho\left(\partial_t \mathbf{u} + \mathbf{u} \cdot \nabla \mathbf{u}\right) = -\nabla p + \mu \nabla^2 \mathbf{u} + \rho\left(T\right)\mathbf{g} \tag{1}$$

where p and T are the fluid pressure and temperature, ρ and μ are the fluid's density and viscosity, respectively, and $\mathbf{g}$ is the gravitational acceleration.

Following standard practice, we use the Boussinesq approximation, retaining the temperature dependence only in the last term to represent the buoyancy force. This is consistent with the assumption of incompressibility, since the relative change in the density due to temperature variation is usually quite small: less than 10% for the vapor and less than 4% for the liquid in the examples considered below. (To verify the validity of this approximation, we also performed the simulations with temperature dependence included for all material parameters and found only minor differences in the results.) Specifically, in the liquid phase

$$\rho_l = \rho_l^*[1 - \beta_l\left(T - T^*\right)], \tag{2}$$

where ρ_l^* is the reference density at the reference temperature T^* and $\beta_l = -(\partial\rho_l/\partial T)/\rho_l$ is the coefficient of thermal expansion. Here and below, subscripts l, v and i denote properties of the liquid and vapor phase, and the liquid-vapor interface, respectively. For the vapor, which is assumed to be an ideal gas,

$$\rho_v = p_v/\bar{R}_v T, \tag{3}$$

where $\bar{R}_v = R/M_v$, R is the universal gas constant, and M_v is the molar mass.

The total mass of fluid in a sealed geometry is conserved,

$$\int_{\text{liquid}} \rho_l dV + \int_{\text{gas}} \rho_v dV = m_t, \tag{4}$$

where m_t is the total mass of the working fluid in both phases. The densities of liquid and vapor are related to the temperature and pressure through (2) and (3). Furthermore, the solution of the Navier-Stokes equation defines the pressure field p up to a constant p_o, so that absolute pressure is

$$p_v = p + p_o, \tag{5}$$

where the pressure offset p_o can be computed from (4):

$$p_o = \left[\int_{\text{gas}} \frac{1}{\bar{R}_v T} dV\right]^{-1} \left[m_t - \int_{\text{liquid}} \rho_l dV - \int_{\text{gas}} \frac{p}{\bar{R}_v T} dV\right]. \tag{6}$$

Finally, the transport of heat is described using an advection-diffusion equation

$$\partial_t T + \mathbf{u} \cdot \nabla T = \alpha \nabla^2 T, \tag{7}$$

where $\alpha = k/\rho C_p$ is the thermal diffusivity, k is the thermal conductivity, and C_p is the heat capacity, of the fluid. The inclusion of advection terms in both transport equations can be justified by computing the Reynolds and thermal Peclet numbers, presented below in Table 5.

2.2. Boundary Conditions

The system of coupled evolution equations for the velocity, pressure, and temperature fields has to be solved in a self-consistent manner, subject to the boundary conditions describing the balance of momentum, heat, and mass fluxes.

Local phase equilibrium between the vapor and the liquid phase is established when the temperature of the vapor at the interface is equal to the saturation temperature. The latter is usually computed using the Clausius-Clapeyron equation

$$\ln \frac{p_v}{p_v^*} = \frac{\mathcal{L}}{\bar{R}_v}\left(\frac{1}{T_s^*} - \frac{1}{T_s}\right), \tag{8}$$

where T_s^* is the saturation temperature at the reference vapor pressure p_v^* and $\mathcal{L}$ is the latent heat of evaporation. In the numerical model we use its generalization (valid over a wider range of temperatures), known as the Antoine equation

$$\log_{10} p_v = A_v - \frac{B_v}{C_v + T_s} \tag{9}$$

where A_v, B_v, and C_v are empirical coefficients. Either (8) or (9) can be also used to define the saturation pressure p_s as a function of temperature.

The heat flux balance across the interface is given by

$$\mathcal{L}J = k_l\, \mathbf{n}\cdot\nabla T_l - k_v \mathbf{n}\cdot\nabla T_v, \tag{10}$$

and the mass flux balance on the vapor side of the interface is

$$J = \rho_v\, \mathbf{n}\cdot(\mathbf{u}_v - \mathbf{u}_i), \tag{11}$$

where $\mathbf{u}_i$ is the velocity of the interface and $\mathbf{n}$ is the unit normal. On the liquid side we can set

$$\mathbf{n}\cdot(\mathbf{u}_l - \mathbf{u}_i) = \frac{J}{\rho_l} \approx 0. \tag{12}$$

since $\rho_l \gg \rho_v$.

Several theoretical models have been put forward to describe the mass flux across the liquid-vapor interface due to phase change. The Kinetic Theory of Gases (KTG) [18] assumes continuous temperature across the liquid-vapor interface, $T_l = T_v = T_i$, and leads to the following expression [19]:

$$J = \frac{2\lambda\rho_v}{2-\lambda}\sqrt{\frac{\bar{R}_v T_i}{2\pi}}\left[\frac{p_l - p_v}{\rho_l \bar{R}_v T_i} + \frac{\mathcal{L}}{\bar{R}_v T_i}\frac{T_i - T_s}{T_s}\right], \tag{13}$$

where λ is the accommodation coefficient, which is usually taken equal to unity. Combining (3), (10), (13) and (9), we can solve for the mass flux J, the interfacial temperature T_i, saturation temperature T_s, and the vapor density at the interface ρ_v.

Several alternative phase change models have been proposed recently which instead predict a discontinuity in the temperature field at the interface. Non-Equilibrium Thermodynamics (NET) [20] leads to the following relations between the mass flux J and the heat flux $q_v = k_v \mathbf{n}\cdot\nabla T_v$ on the vapor side:

$$\frac{p_s - p_v}{\sqrt{2\pi\bar{R}_v T_l}} = r_{11} J + r_{12}\frac{q_v}{\bar{R}_v T_l}, \tag{14}$$

$$\frac{p_s}{\sqrt{2\pi\bar{R}_v T_l}}\frac{T_l - T_v}{T_l} = r_{21} J + r_{22}\frac{q_v}{\bar{R}_v T_l}, \tag{15}$$

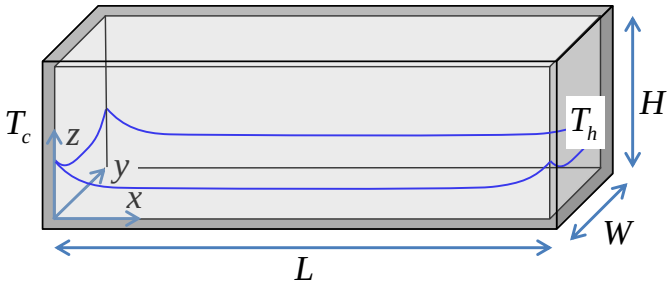

Figure 1: The test cell containing the liquid and vapor or air/vapor mixture. Gravity is pointing in the negative z direction. The shape of the contact line reflects the curvature of the free surface.

where T_l and T_v are the interfacial temperatures on the liquid and vapor side, respectively, and $p_s(T_l)$ is determined from (9). The dimensionless resistivities r_{ij} are obtained from the Onsager reciprocity relation. If the vapor behaves as an ideal gas with accommodation (condensation) coefficient λ, their values can be obtained using kinetic theory of gases [21]: $r_{11} = \lambda^{-1} - 0.40044$, $r_{12} = r_{21} = 0.126$, and $r_{22} = 0.294$.

Equations (3), (9), (10), (14) and (15) can then be solved to determine the mass flux J, the interfacial temperature T_l at the liquid side and T_v at the vapor side, the vapor density ρ_v at the interface, and the saturation pressure p_s. The normal component of the vapor velocity at the interface $\mathbf{n}\cdot\mathbf{u}_v$ can again be obtained from J using (11).

Finally, the mass flux can also be computed using Statistical Rate Theory (SRT) [22], which predicts

$$J = 2\frac{p_s}{\sqrt{2\pi\bar{R}_v T_l}}\left[\frac{p_s - p_v}{\rho_l \bar{R}_v T_l} + \frac{2\kappa\sigma}{\rho_l \bar{R}_v T_l} - 2\left(\frac{T_v}{T_l} - 1\right)^2\right], \tag{16}$$

where κ is the interfacial curvature and $p_s(T_l)$ is again determined by (9). We can then solve for the mass flux J, the interfacial temperature T_l at the liquid side and T_v at the vapor side, and the vapor density ρ_v at the interface using equations (3), (9), (10), and (16).

The remaining boundary conditions at the liquid-vapor interface are standard: the tangential velocity components are considered continuous

$$(1 - \mathbf{n}\cdot\mathbf{n})\cdot(\mathbf{u}_l - \mathbf{u}_v) = 0. \tag{17}$$

The stress balance

$$(\Sigma_l - \Sigma_v)\cdot\mathbf{n} = \mathbf{n}\kappa\sigma + \nabla_s\sigma = \mathbf{n}\kappa\sigma - \gamma\nabla_s T_i \tag{18}$$

incorporates both the viscous drag between the two phases and the thermocapillary effects. Here $\Sigma = \mu\left[\nabla\mathbf{u} - (\nabla\mathbf{u})^T\right] - p$ is the stress tensor, $\nabla_s = (1 - \mathbf{n}\cdot\mathbf{n})\cdot\nabla$ is the surface gradient, and $\gamma = -\partial\sigma/\partial T$ is the temperature coefficient of surface tension.

We further assume that the fluid is contained in a rectangular cavity (see Fig. 1) with thin poorly conducting end walls (of thickness h_w and conductivity k_w). The left wall is "cooled" with a constant temperature T_c imposed on the outside, while the right wall is "heated" with a constant temperature $T_h > T_c$ imposed on the outside. Since the walls are thin,

one-dimensional conduction is assumed, yielding the following boundary conditions on the inside of the side walls:

$$T|_{x=0} = T_c + \frac{k_n}{k_w} h_w \, \mathbf{n} \cdot \nabla T, \tag{19}$$

$$T|_{x=L} = T_h + \frac{k_n}{k_w} h_w \, \mathbf{n} \cdot \nabla T, \tag{20}$$

where $n = g$ ($n = l$) above (below) the contact line.

The heat flux through the top, bottom, front and back walls is ignored (adiabatic boundary conditions are typical of most experiments). Standard no-slip boundary conditions $\mathbf{u} = 0$ for the velocity are imposed on all the walls and the boundary condition on the pressure

$$\mathbf{n} \cdot \nabla p = \rho(T) \, \mathbf{n} \cdot \mathbf{g} \tag{21}$$

follows from (1).

3. Results and Discussion

The model described above has been implemented numerically by adapting an open-source general-purpose CFD package OpenFOAM [23] to solve the governing equations in both 2D and 3D geometries. Details are available in Ref. [3].

In this section, we will use the computational model to investigate the buoyancy-thermocapillary flow of a fluid confined in a sealed rectangular test cell used in the experimental study of Li *et al.* [2]. The working fluid is hexamethyldisiloxane, a silicone oil with a kinematic viscosity $\nu = 0.65$ cSt, which is a volatile liquid with the properties summarized in Table 1. A layer of liquid of average thickness $d_l = 2.45$ mm is confined in the test cell with the inner dimensions $L \times H \times W = 48.5$ mm $\times 10$ mm $\times 10$ mm (see Fig. 1), below a layer of vapor. The walls of the test cell are made of quartz (fused silica) with thermal conductivity $k_w = 1.4$ W/m-K and have thickness $h_w = 1.25$ mm. Though the silicone oil wets quartz very well, we set the contact angle $\theta = 50^\circ$ here to avoid numerical instabilities. This has a minor effect on the shape of the free surface everywhere except very near the contact lines.

While the numerical model can describe the flows in both 2D and 3D systems, the results presented here are obtained for 2D flows (ignoring variation in the y-direction), since 3D simulations require significant computational resources and comparison of 2D and 3D results for the same system under air at atmospheric conditions were essentially identical [3]. The 2D system corresponds to the central vertical (x-z) plane of the test cell.

Initially, the fluid is assumed stationary with uniform temperature $T_0 = (T_c + T_h)/2$ ($T_0 = 293$ K in all cases), the liquid layer is of uniform thickness (such that the liquid-gas interface is flat), and the pressure in the vapor layer p_v is set equal to the saturation pressure at T_0, $p_s(T_0) \approx 4.3$ kPa, calculated from (9). As the system evolves towards an asymptotic state, the flow develops in both phases, the interface distorts to accommodate the assigned contact angle at the walls, and a temperature gradient in both phases is established. The simulations are first performed on a coarse hexahedral mesh (initially all cells are cubic with a dimension of 0.5 mm), since the initial transient state is of secondary interest. Once the transient dynamics have died down, the simulations are continued after the mesh is refined in several steps, until the results become mesh independent.

	liquid	vapor
μ (kg/(m·s))	4.95×10^{-4}	6.0×10^{-6}
ρ (kg/m^3)	761.0	0.275
β (1/K)	1.34×10^{-3}	$1/T$
k (W/(m·K))	0.1	0.03
α (m^2/s)	9.52×10^{-8}	9.08×10^{-5}
Pr	6.83	0.24
σ (N/m)	1.59×10^{-2}	
γ (N/(m·K))	7×10^{-5}	
$\mathcal{L}$ (J/kg)	2.14×10^5	

Table 1: Material properties at the reference temperature $T_0 = 293$ K. In the vapor phase, the coefficient of thermal expansion $\beta = 1/T$ based on the ideal-gas assumption.

3.1. Fluid Flow and Temperature Fields

Simulations were performed at temperature differences ΔT ranging from 10 K to 30K using the KTG expression for the evaporation/condensation mass flux (13) with accommodation coefficient $\lambda = 1$. For this range of ΔT, under atmospheric conditions, the flow is found to transition from steady unicellular to steady multicellular to oscillatory convection [3], as Fig. 2 illustrates. In the absence of noncondensables, at otherwise identical conditions, the flow was found to reach steady state for all of these values of ΔT. The corresponding streamlines in both the liquid and the vapor phase are shown in Fig. 3. The flow in the liquid layer is markedly different under vapor and under air. Under air the flow in the central region of the cell is best described as a horizontal return flow with multiple embedded convection rolls whose strength increases progressively with ΔT. In this case thermocapillarity is the dominant driving force [3]. The flow under vapor looks qualitatively the same over this range of ΔT and is dominated by two counter-clockwise convection rolls, a larger one near the cold wall and a smaller one near the hot wall. The flow is much stronger near the end walls than in the central region, suggesting that the main driving force in buoyancy, rather than thermocapillarity.

The flow in the vapor phase is also qualitatively different. Under air we find a (clockwise) recirculation flow in the vapor phase which mirrors the flow in the liquid phase. It is driven primarily by thermocapillarity, with buoyancy causing counter-clockwise recirculation in the top corners. In the absence of air, the flow in the vapor phase becomes unidirectional, with the liquid evaporating near the hot wall, vapor flowing from the hot wall to the cold wall and condensing there. Again, increasing ΔT has essentially no effect on the structure of the flow field. The observation from the numerics that the convection pattern is independent of applied temperature difference, at least qualitatively, is consistent with recent experimental results [2] which show that transitions from steady unicellular to steady multicellular to oscillatory convection observed under atmospheric conditions disappear when (most of) the air is removed.

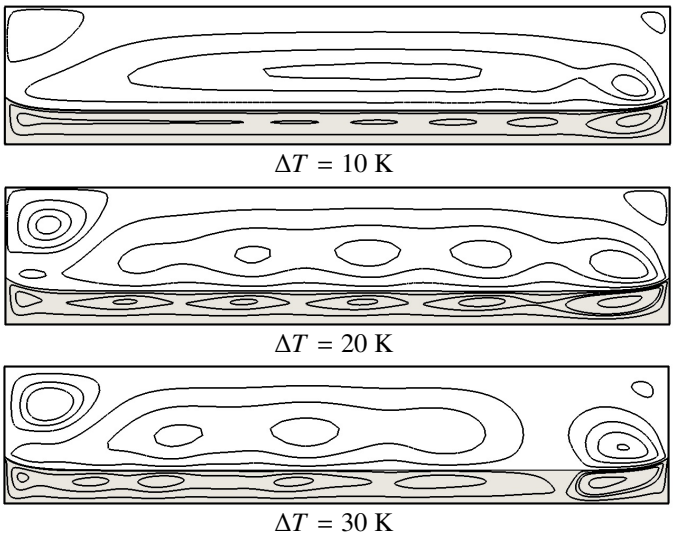

Figure 2: Streamlines of the flow under air for different ΔT, reproduced from Ref. [3]. The gray background indicates the liquid phase, the white background the gas phase. The contact angle is $\theta = 50°$. The flow at $\Delta T = 30$ K is time-periodic; a particular (representative) time instance is shown.

	under vapor			under air		
ΔT (K)	$\langle\|\mathbf{u}_i\|\rangle_x$ (mm/s)	u_B (mm/s)	u_T (mm/s)	$\langle\|\mathbf{u}_i\|\rangle_x$ (mm/s)	u_B (mm/s)	u_T (mm/s)
10	0.6	1.3	0.004	6	1.3	5.3
20	0.9	2.6	0.009	9.4	2.6	7.9
30	1.5	3.8	0.013	11.6	3.8	10.7

Table 2: The spatial average of the interfacial velocity $\langle|\mathbf{u}_i|\rangle_x$ and the estimates of thermocapillary and buoyancy contributions based on (35) and (36). A time-averaged value is given for the time-periodic flow under air at $\Delta T = 30$ K.

Table 2 summarizes the average interfacial velocities predicted by the numerical model (along with the analytical estimates derived below) for different values of ΔT. Not only are the flow patterns under air and under vapor significantly different, but the magnitude of the velocity is quite different as well. While under air the flow is relatively fast (the largest interfacial velocity is of order a few cm/s for $\lambda = 1$), under vapor the flow is predicted to be much slower (the largest interfacial velocity is reduced to a few mm/s, for the same value of λ). In order to understand this rather significant reduction in the flow velocity it is helpful to compare the temperature fields in the two cases.

Figure 4 shows the isotherms for both cases when applied temperature difference is $\Delta T = 10$ K. Under air, the temperature changes in a relatively smooth manner between the hot end and the cold end in both phases. Under vapor, the isotherms are clustered near the "hot" and "cold" end walls, indicating the formation of sharp thermal boundary layers near the end walls, with the temperature being nearly constant in the central region of the cell. Moreover, the temperature appears to be essentially constant along the entire interface. This would suggest that thermocapillarity will be significantly reduced in the case under vapor. Indeed, for a liquid in equilibrium with its vapor, the interfacial temperature is set by the saturation temperature, which depends only on the *absolute* pressure. Since the latter is

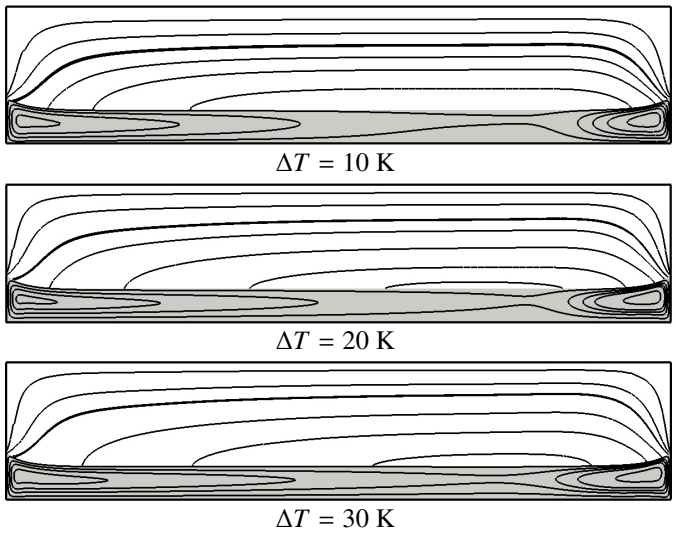

Figure 3: Streamlines of the flow under pure vapor for different ΔT. The gray background indicates the liquid phase, the white background the vapor phase. The contact angle is $\theta = 50°$.

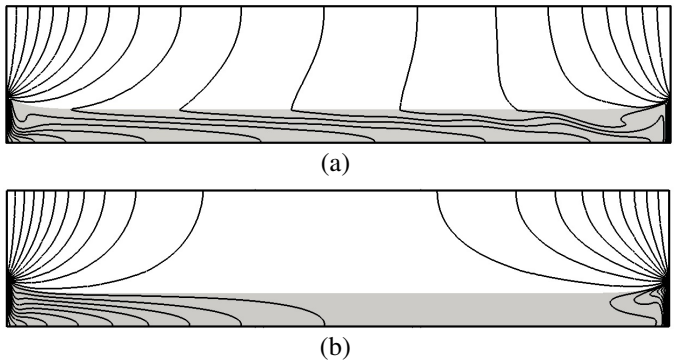

Figure 4: Temperature field for the steady-state flows (a) under air [3] and (b) under vapor. In both cases $\Delta T = 10$ K, the gray background indicates liquid, the white background the vapor. The temperature difference between adjacent isotherms is 0.5 K.

effectively constant, so is the interfacial temperature. We will look at this in detail next.

3.2. Interfacial Temperature

The variation of the temperature T_i at the interface between the liquid and gas phase (about its average value $\langle T_i\rangle_x \approx T_0$) is shown in Fig. 5. When the system is under air at atmospheric pressure, $T_i(x)$ is described by a nearly periodic modulation about a linear profile over most of the interface, as observed, for instance, in the experiments of Riley and Neitzel [7]. The modulation corresponds to the advection of heat by convective flow and the average value of the temperature gradient $\tau = \partial T_i/\partial x$ is comparable to the value of the imposed temperature gradient $\Delta T/L$. In the absence of air, the interfacial temperature becomes essentially constant. The value of τ, and the corresponding thermocapillary stresses, decrease by three orders of magnitude, compared with the values found under air at the same ΔT.

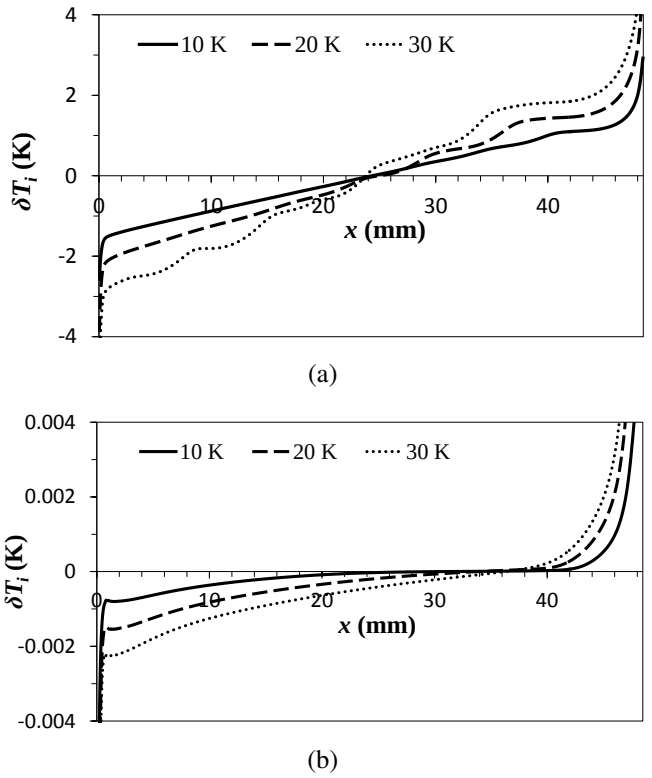

Figure 5: Interfacial temperature (a) under air [3] and (b) under vapor. To amplify the variation of T_i in the central region of the cell we plotted the variation $\delta T_i = T_i - \langle T_i \rangle_x$ about the average and truncated the y-axis.

This drastic reduction in the magnitude of τ can be understood using a simple argument. In the absence of noncondensables, the diffusion of vapors does not inhibit phase change, so the interfacial temperature should be very close to the saturation temperature due to the large value of latent heat in (13). On the other hand, T_s is a function of the vapor pressure p_v, which is nearly constant. Hence T_s is nearly constant, and so is T_i.

A quantitative estimate for the variation of T_i in the two limits can be obtained by a straightforward analysis of the theoretical model. Using (13) the interfacial temperature can be written as

$$T_i \approx T_s + \underbrace{\frac{2-\lambda}{2\lambda}\sqrt{\frac{2\pi}{\bar{R}_v T_s}}\frac{\bar{R}_v T_s^2}{\rho_v \mathcal{L}} J}_{T_p} - \underbrace{\frac{T_s}{\rho_l \mathcal{L}}(p_l - p_v)}_{T_c}. \tag{22}$$

The variation $\Delta T_i \sim \tau L$ in the interfacial temperature over the central portion of the cell can be computed by adding the contributions describing the variations ΔT_s, ΔT_p, and ΔT_c, of the three terms on the right hand side of (22). These terms describe the effect of variation in the saturation pressure, phase change, and interfacial curvature, respectively.

Let us start with the last term, ΔT_c. Since the fluid velocities are very low, the pressure jump across the interface is determed by the Young-Laplace pressure $|p_l - p_v| \approx \kappa\sigma$, where the curvature of the interface is of order the inverse of the capillary length scale, $\kappa \sim \sqrt{\rho_l g/\sigma}$. Furthermore, $T_s \approx T_0$, so the temperature variation due to the curvature of the interface is

$$\Delta T_c \sim \frac{T_0}{\mathcal{L}}\sqrt{\frac{\sigma g}{\rho_l}} \approx 2 \times 10^{-5}\ \text{K}, \tag{23}$$

irrespective of the presence or absence of noncondensables.

The magnitude of the temperature variation ΔT_p due to the latent heat absorbed or released at the interface is controlled by the variation ΔJ in the mass flux, which describes the phase change at the interface. In the absence of noncondensables, the rate of phase change is limited by the diffusive heat flux in the region adjacent to the hot (cold) end wall. The relevant length scale is the thickness of the liquid layer d_l and the relevant temperature scale is $\Delta T/2$. Ignoring the negligible heat flux in the gas phase and using (10) we find

$$\Delta J \sim \frac{k_l}{\mathcal{L}}\frac{\Delta T}{2d_l}. \tag{24}$$

Substituting the properties of the working fluid gives $\Delta J \sim 10^{-3}$ kg/(m^{2}s) for $\Delta T = 10$ K, which is consistent with the values found near the end walls numerically (cf. Fig. 6(b)). With the typical (for a non-polar liquid) choice $\lambda = 1$

$$\Delta T_p \sim \frac{2-\lambda}{4\lambda}\sqrt{\frac{2\pi}{\bar{R}_v T_0}}\frac{\bar{R}_v T_0^2}{\rho_v \mathcal{L}}\Delta J \tag{25}$$

yields $\Delta T_p \sim 10^{-3}$ K.

When the gas phase is dominated by noncondensables (air), phase change will be suppressed, since vapor has to diffuse towards/away from the interface. In this case the mass flux across the interface is limited by diffusion and the variation in the mass flux can be estimated as

$$\Delta J \sim D\,|\mathbf{n}\cdot\nabla\rho_v| \sim D\frac{\Delta\rho_v}{2d_l}, \tag{26}$$

where D is the diffusion constant and $\Delta\rho_v$ is the variation of the vapor density, which can be estimated from the equilibrium values of the vapor pressure at T_h and T_c. With the help of (3) and (8) we find

$$\Delta\rho_v \sim \frac{\partial\rho_v}{\partial p_v}\frac{\partial p_v}{\partial T}\Delta T \sim \frac{\mathcal{L} p_v}{\bar{R}_v^2 T_0^3}\Delta T \tag{27}$$

and therefore

$$\Delta J \sim D\,\frac{\mathcal{L} p_v}{\bar{R}_v^2 T_0^3}\frac{\Delta T}{2d_l}. \tag{28}$$

For $\Delta T = 10$ K this estimate gives $\Delta J \sim 7 \times 10^{-4}$ kg/(m^{2}s). A more accurate estimate can be obtained by using the variation of temperature along the interface $\Delta T_i \approx \tau L$ instead of ΔT in (28), which yields a lower value $\Delta J \sim 2 \times 10^{-4}$ kg/(m^{2}s) that is in better agreement with the numerical result (cf. Fig. 6(a)). However, for the purposes of estimating ΔT_i the former, less accurate, estimate is sufficient and gives $\Delta T_p \sim 10^{-3}$ K.

Finally, the magnitude of the variation in the saturation temperature ΔT_s is controlled by the variation of the vapor pressure Δp_v, which differs greatly in the two limits considered here. When the gas phase is pure vapor, the vapor pressure is equal to

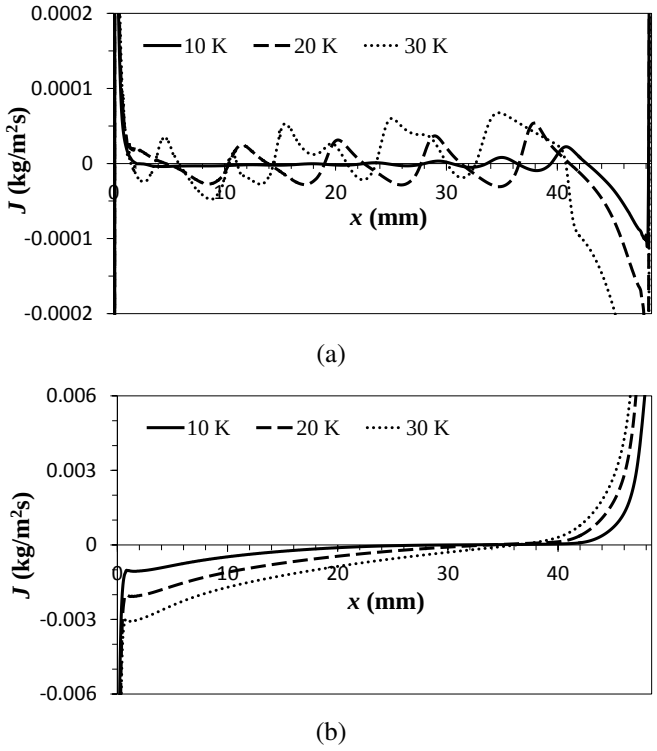

Figure 6: Mass flux for different ΔT (a) under air [3] and (b) under vapor. The y-axis is truncated so that the details of the variation in the core region of the flow can be seen.

the absolute pressure in the gas phase. The variation of the absolute pressure along the liquid-gas interface can be estimated using the pressure drop for the flow of viscous vapor. The flow has an approximately Poiseuille profile between two infinitely large parallel planes formed by the top wall and the liquid-vapor interface, with the separation equal to the vapor layer thickness d_v. The vapor speed is much larger than that on the liquid-vapor interface, so both planes can be assumed stationary. The volumetric flow rate per unit width (in the y direction) can be estimated by integrating the phase change mass flux over the region of intense evaporation (which has a width of order d_l) $Q \sim \Delta J d_l/\rho_v$ yielding

$$\Delta p_v \sim 12\frac{\mu_v Q L}{d_v^3} \sim 12\frac{\mu_v d_l L}{\rho_v d_v^3}\Delta J, \tag{29}$$

which together with (3) and (8) gives

$$\Delta T_s = \frac{\partial T_s}{\partial p_v}\Delta p_v \sim 12\frac{\mu_v d_l L T_0}{\rho_v^2 d_v^3 \mathcal{L}}\Delta J. \tag{30}$$

Using the estimate (24) for ΔJ gives $\Delta T_s \sim 2\times 10^{-6}$ K.

In the presence of noncondensables, vapor pressure is equal to the partial pressure instead of the absolute pressure. With the help of (3), (8) and (27) we find

$$\Delta T_s = \frac{\partial T_s}{\partial p_v}\frac{\partial p_v}{\partial \rho_v}\Delta\rho_v \sim \frac{\bar{R}_v T_0^2}{\mathcal{L} p_v}\bar{R}_v T_0 \frac{\mathcal{L} p_v \Delta T}{\bar{R}_v^2 T_0^3} = \Delta T, \tag{31}$$

so that, in this case, it is the imposed temperature difference ΔT that sets the scale for the variation in T_s.

	ΔT_s (K)	ΔT_p (K)	ΔT_c (K)	ΔT_i (K)
under vapor	2×10^{-6}	2×10^{-3}	2×10^{-5}	2×10^{-3}
under air	10	1×10^{-3}	2×10^{-5}	10

Table 3: Estimates of how various physical effects contribute to the variation in the interfacial temperature T_i, for $\Delta T = 10$ K.

Table 3 summarizes the estimates that quantify the contributions of different physical effects to the variation of the interfacial temperature. Clearly, the dominant physical effect is different for the two limiting cases considered here. Under pure vapor, $\Delta T_s \ll \Delta T_c \ll \Delta T_p$, so that the variation in T_i is mainly due to the latent heat released or absorbed at the interface. However, despite the absence of noncondensables that hinder phase change, this is a fairly weak effect: the resulting variation $\Delta T_i \approx \Delta T_p$ is almost four orders of magnitude less than the imposed temperature difference ΔT. Under air, $\Delta T_c \ll \Delta T_p \ll \Delta T_s$, so that the variation in T_i is mainly due to the variation of the saturation temperature, $\Delta T_i \approx \Delta T_s \sim \Delta T$. Both estimates are in good agreement with the numerical results presented in Fig. 5.

These estimates have a number of other interesting corollaries. For instance, while our earlier numerical results show that Newton's Law of Cooling

$$\mathbf{n}\cdot\nabla T_l = Bi\frac{T_i - T_0}{d_l} \tag{32}$$

(where Bi is the Biot number) completely breaks down under air [3], the law appears to be somewhat accurate under vapor. Indeed, in the absence of air, heat conduction in the gas layer can be ignored, so the heat flux balance relation (10) simply reduces to

$$\mathcal{L}J \approx k_l\,\mathbf{n}\cdot\nabla T_l. \tag{33}$$

Furthermore, ΔT_c and ΔT_s are negligible compared to ΔT_p, so that we can set $T_c = 0$ and $T_s = T_0$ in (22), which yields (32) with $Bi = E$, where

$$E = \frac{2\lambda}{2-\lambda}\sqrt{\frac{\bar{R}_v T_0}{2\pi}}\frac{\rho_v \mathcal{L}^2 d_l}{k_l \bar{R}_v T_0^2} \tag{34}$$

is the nondimensional evaporation number defined as the ratio of the latent heat flux at the interface to the conductive heat flux in the liquid [17].

For the conditions of the present study $E = 6.9\times 10^3$. Figure 7 shows the local Biot number computed for the numerical solutions in the two limits. The local values of Bi under vapor are indeed comparable to the theoretical estimate (34) over the entire x interval. In contrast, under air Bi not only exhibits significant variation, it even changes sign, indicating that there is no correlation between the deviation of the interfacial temperature from some average value and the normal component of the temperature gradient in the liquid layer.

The magnitude of the flow velocity at the interface can be estimated with the help of the analytical solution for the uniform flow in an unbounded fluid layer originally derived by Birikh [24] (and later rederived by Kirdyashkin [25] and Villers and

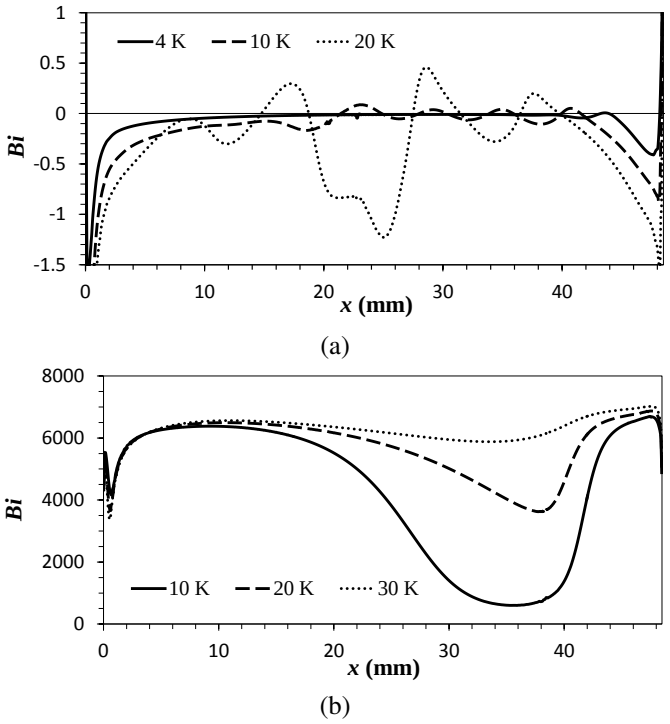

Figure 7: Local Biot number computed using (32) for different ΔT (a) under air [3] and (b) under vapor. Under vapor we set T_0 as the interfacial temperature at the point where $\mathbf{n} \cdot \nabla T_l = 0$, while under air $T_0 = (T_c + T_h)/2$.

Platten [26]). The two terms in the solution give the contribution due to thermocapillary

$$u_T = \frac{1}{4}\frac{\nu_l}{d_l} Pr^{-1} Ma_i \tag{35}$$

and due to buoyancy

$$u_B = \frac{1}{48}\frac{\nu_l}{d_l} Pr^{-1} Ra, \tag{36}$$

where $Pr = \nu_l/\alpha_l$ is the Prandtl number,

$$Ma_i = \frac{\gamma d_l^2 \tau}{\mu_l \alpha_l} \tag{37}$$

is the interfacial Marangoni number,

$$Ra = \frac{g\beta_l d_l^4 \Delta T}{\nu_l \alpha_l L} \tag{38}$$

is the Rayleigh number and $\nu_l = \mu_l/\rho_l$ is the kinematic viscosity of the liquid. It should be noted that our definition of Ra differs from the one used, e.g., in Refs. [3, 7]. The reason is that, while u_T is controlled by the interfacial temperature gradient $\tau \sim \Delta T_i/L$, u_B is controlled by the imposed temperature difference ΔT, which sets the vertical temperature variation in the liquid layer both under air and under vapor. For the range of ΔT considered here, τ and ΔT are not related in any simple way. For instance, under air the relationship is nonlinear: $\Delta T/L$ is a low-order rational function of τ [3].

While u_T is sensitive to the presence of noncondensables, u_B is not. The ratio of the two velocities is

$$\frac{u_T}{u_B} \approx 12 \frac{L\tau}{\Delta T} Bo_D^{-1}, \tag{39}$$

	under vapor			under air		
ΔT (K)	10	20	30	10	20	30
$Ra \times 10^{-4}$	3.1	6.2	9.4	3.1	6.2	9.4
Ma_i	0.45	0.89	1.34	547	804	1096
Bo_D	0.853					
$L\tau/\Delta T$	1.3×10^{-4}			0.3	0.22	0.2

Table 4: The values of nondimensional parameters for the numerical solutions under vapor and under air [3].

	Re_l	Re_v	Pe_l	Pe_v
under vapor	2.3	4	15.7	0.95
under air	23.1	3.5	157.3	2.4

Table 5: Reynolds and thermal Peclet numbers for the liquid and the gas phase under vapor and under air at ΔT =10 K.

where the dynamic Bond number

$$Bo_D = \frac{\beta_l \rho_l g d_l^2}{\gamma} \tag{40}$$

is 0.853 for the liquid layer of average thickness d_l = 2.45 mm considered here. In the experiments of Li *et al.* [2], d_l is comparable to this value, with Bo_D ranging from 0.85 to 1.0. The values of various nondimensional parameters are summarized in Tables 4 and 5. Under air $L\tau/\Delta T$ varies from about 0.2 to 0.3 for ΔT between 10 K and 30 K, so the flow is dominated by thermocapillary, $u \approx u_T$. Under vapor $L\tau/\Delta T \ll 1$, so the flow is dominated by buoyancy, $u \approx u_B$ and should be slower by a factor of 2.8 to 4.2, compared with the flow at the same ΔT under air. Overall, these estimates are consistent with the numerical results presented in Table 2, although the numerically computed flow speeds under vapor are even smaller than u_B, since the flow profile differs substantially from the analytical solution on which the estimate (36) is based.

The experiments, on the other hand, paint a completely different picture [2]. To facilitate the comparison, we summarized the experimental results in Table 6 in terms of the corresponding interfacial Marangoni and dynamic Bond numbers. Unlike the numerical results and analytical estimates, in the experiment the values of Ma_i and the corresponding interfacial velocities under vapor are comparable to, and even slightly higher than, those under air. Since buoyancy is unaffected by the presence of noncondensables, this implies that the thermocapillary stresses and hence the interfacial temperature gradient τ in the experiment should be essentially the same at atmospheric conditions and when most of the air has been removed.

In the conclusion of this section let us point out that, as Fig. 5 illustrates, the interfacial temperature varies much more rapidly

	under vapor		under air	
ΔT (K)	3.9	11.6	3.8	11.5
Ma_i	460	790	370	690
Bo_D	1.0	0.89	0.89	0.85

Table 6: The values of nondimensional parameters for the experiments reported in Ref. [2] under vapor and under air.

near the end walls than in the central portion of the cell, changing by $\delta T = O(\Delta T)$ across very narrow boundary layers. The width δx of these boundary layers can be estimated by noting that contact lines correspond to the stagnation points of the flow. Hence heat transport in the boundary layers is dominated by conduction and, since $k_v \ll k_l$ both under vapor and under air, the right-hand-side of (10) can be estimated as $k_l \delta T/\delta x$, which gives the estimate $J \sim (k_l \delta T)/(\mathcal{L}\delta x)$ for the mass flux near the contact line. On the other hand, this mass flux can also be estimated using (13). Evaluated at the interface, T_s changes very little across the boundary layer, while outside the boundary layer $T_s \approx T_i$. Hence we can set $T_i - T_s \sim \delta T$ in the second term on the right-hand-side of (13) and ignore the first (curvature) term. Equating the two estimates yields the boundary layer thickness [27]

$$\delta x \sim E^{-1} d_l, \tag{41}$$

where E is the evaporation number defined by (34). Evaluating this for the present case, we obtain $\delta x \sim 0.36\ \mu$m, which is two orders of magnitude less than the spatial resolution of the finest computational mesh used here, explaining the singular behavior of J and T_i in the vicinity of the contact lines.

3.3. Comparison of Different Phase Change Models

Our analysis of the KTG-based model shows that significant gradient of the interfacial temperature can only be established when noncondensables impede the transport of vapor from the hot end to the cold end of the cell. Hence, when air is removed completely from the test cell, thermocapillary stresses are dramatically suppressed. The experiment, however, shows that the observed flow velocity is comparable in the two limiting cases [2], raising the question about the cause of the thermocapillary stresses which arise under vapor. One possibility, considered below, is that the KTG prediction breaks down under intense phase change and a different theoretical model has to be used to describe phase change in the (near) absence of noncondensables. Indeed, SRT and NET predict a temperature jump across the liquid-vapor interface, which could, in principle, lead to a variation in the temperature of the liquid that exceeds the variation of the temperature of the gas at the interface, and hence produce stronger thermocapillary stresses. Some experimental studies report temperature jumps across the interface as high as 3 K for unforced evaporation and as high as 10-20 K for evaporation of heated layers of water [28, 29, 30].

We have computed the steady state flows under vapor for $\Delta T = 10$ K using three different models of phase change. For KTG and NET we set the accommodation coefficient $\lambda = 1$ following the vast majority of theoretical studies. The corresponding mass flux J is shown in Fig. 8. Quite interestingly, the spatial profile of J is independent of the choice of the model – the three curves are indistinguishable. The temperature profiles on the liquid side of the interface shown in Fig. 9(a) are also very similar, especially for KTG and SRT. The interfacial temperature profile for NET deviates slightly from those for KTG and SRT near the end walls, but this deviation is quite small in absolute terms – less than 10^{-3} K. Most importantly, all three

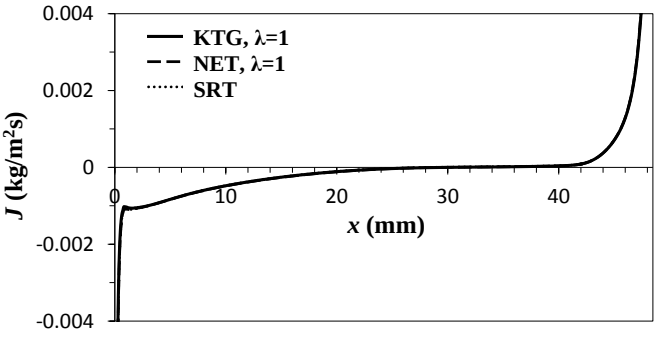

Figure 8: Mass flux for $\Delta T = 10$ K. The accommodation coefficient is $\lambda = 1$ for KTG and NET. The y-axis is truncated so that the details of the variation in the core region of the flow can be seen.

models are consistent with the estimates derived in the previous section. In other words, all three models unequivocally predict that the thermocapillary stresses should essentially disappear when the noncondensables are removed from the cell.

NET and SRT both predict that the temperature field is not continuous across the interface. Fig. 10 shows the temperature jump $T_l - T_v$ computed numerically for these two phase change models. Here we do find a notable difference. NET predicts a substantially larger temperature jump than SRT. For NET the largest temperature jump occurs near the cold (hot) wall where vapor condenses (liquid evaporates) and reaches values of 0.6 K (-0.6 K). For SRT the largest temperature jump is also found near the end walls, but is considerably smaller, with values of only 0.02 K (-0.02 K). Indeed, the variation of the vapor temperature along the interface far exceeds the variation of the liquid temperature along the interface, although both are substantially less than the imposed temperature difference ΔT. This means that KTG provides a reasonably accurate description of the phase change process and the temperature can be assumed continuous across the interface without introducing significant errors.

3.4. Dependence on the Accommodation Coefficient

Another possible explanation for the discrepancy between the model predictions and the experimental observations is an incorrect value of the accommodation coefficient λ. As discussed earlier, $\Delta T_i \approx \Delta T_p$ under vapor. Assuming that the mass flux J is independent of the details of the phase change model (and, in particular, the choice of λ), from (25) it follows that

$$\Delta T_i \propto f(\lambda) = \frac{2}{\lambda} - 1 \tag{42}$$

for small values of λ. While there are no reliable values for the accommodation coefficient reported in the literature for the 0.65 cSt silicone oil, values as low as 10^{-2} have been reported for water [29, 31, 32]. We therefore repeated the numerical simulations for $\lambda = 0.05$, which is most likely substantially less than the actual value for the silicone oil (which is a non-polar liquid), to quantify the dependence of our results on the accommodation coefficient. According to (42), this should increase ΔT_i by a factor of $2/\lambda \approx 40$.

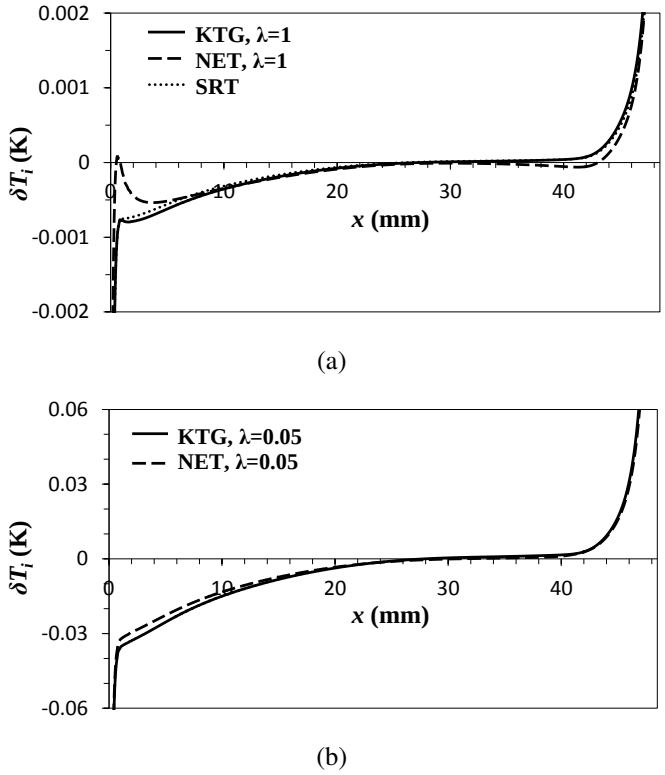

Figure 9: Interfacial temperature profiles for $\Delta T = 10$ K. Plotted is the deviation $\delta T = T_i - \langle T_i \rangle_x$ from the average value (on the liquid side for NET). For KTG and NET, the accommodation coefficient is unity in (a) and 0.05 in (b).

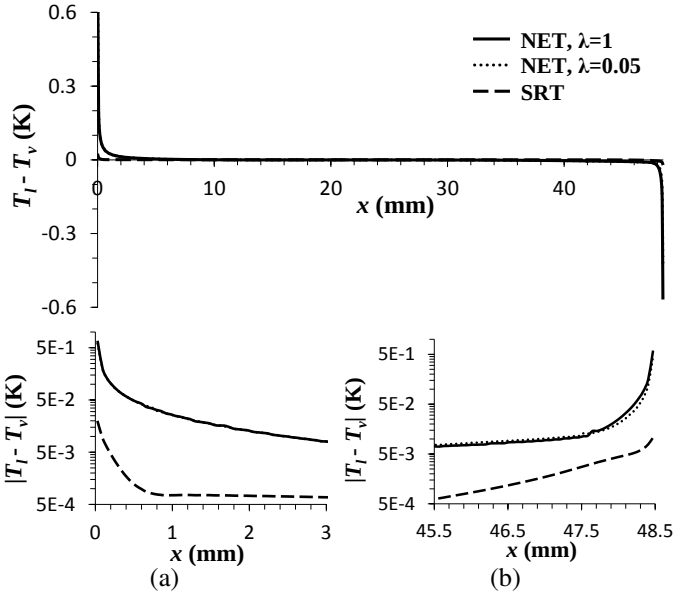

Figure 10: Temperature jump across the interface for $\Delta T = 10$ K. The two panels at the bottom show the regions near the end walls.

The results of numerical simulations presented in Fig. 11 show that the mass flux J is independent not only of the choice of the phase change model, but also of the value of λ. This result can be easily rationalized by generalizing the argument which lead to the relation (24) between the overall variation ΔJ and the heat flux through the liquid layer. In the absence of noncondensables the heat flux through the gas layer is negligibly small, while the interfacial temperature is effectively constant. Under these conditions, thermocapillarity is negligible and the flow in the liquid layer is governed solely by buoyancy. This flow, along with the heat conduction through the liquid, determines the temperature distribution, and hence the conductive heat flux $k_l \mathbf{n} \cdot T_l \approx \mathcal{L} J$, along the entire interface.

Fig. 9(b) compares the interfacial temperature T_i computed using KTG and NET for $\lambda = 0.05$. The interfacial temperature profiles are even more similar in this case than the profiles for the same two models at $\lambda = 1$ shown in Fig. 9(a). As expected, the interfacial temperature variation ΔT_i increases rather significantly as λ decreases from unity to 0.05.

To quantify the changes in the interfacial temperatures associated with the changes in the accommodation coefficient, the data from Fig. 9 were replotted in Fig. 12, which shows the temperature variation $\delta T_i = T_i - \langle T_i \rangle_x$ about the mean rescaled by the dimensionless factor $f(\lambda)$. Aside from the spike near the cold wall for NET with $\lambda = 1$, the scaled interfacial temperature profiles are essentially independent of both the model and the value of λ. This means that ΔT_i does indeed scale with $f(\lambda)$, as predicted previously. While ΔT_i increases as λ decreases, in order to achieve ΔT_i of order ΔT the value of λ has to be reduced to about 10^{-3} which, for silicone oil, appears unphysical. Hence, the only logical conclusion is that an improper choice of the value of the accommodation coefficient also fails to account for the discrepancy between theoretical predictions and experimental observations.

Finally, note that while the value of the accommodation coefficient does affect the variation of T_i *along* the interface, it does not affect the temperature jump $T_l - T_v$ *across* the interface. Fig. 10 shows that the temperature jump, along the entire interface, is independent of the value of λ.

4. Conclusions

We have developed, implemented, and validated a comprehensive numerical model of two-phase flows of confined volatile fluids, which accounts for momentum, mass, and heat transport in both phases and phase change at the interface. This model was used to investigate buoyancy-thermocapillary convection in a sealed cavity subject to a horizontal temperature gradient at dynamic Bond numbers of order unity, in the absence of noncondensables such as air. The results were compared with numerical results obtained previously for the same system in the presence of air at atmospheric pressure as well as with the experimental results in the system where most (but not all) of the air was removed.

The presence of noncondensable gases was found, as expected, to have profound effects on the heat and mass transfer. The numerical results show that the convection patterns are significantly different in the complete absence of air and in the presence of air at atmospheric pressure. The difference is due to the thermocapillary stresses which essentially disappear

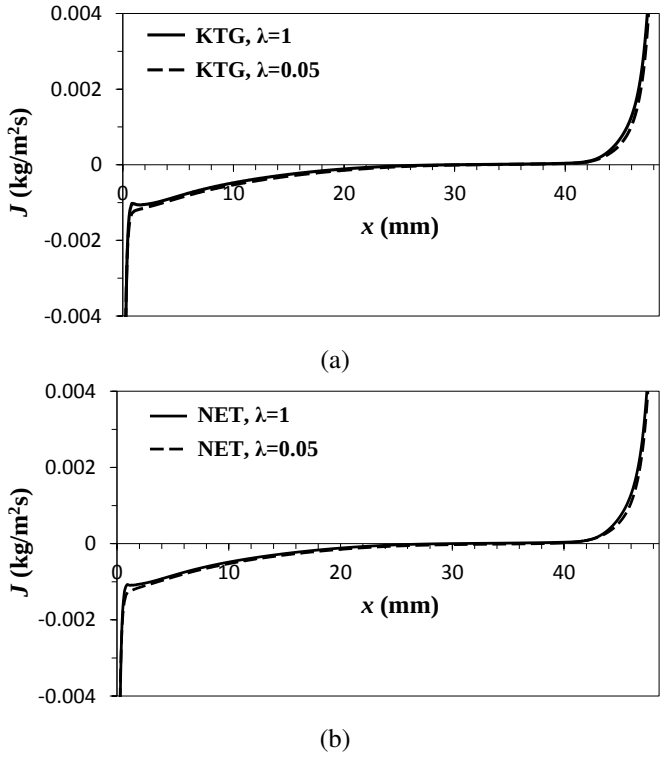

Figure 11: Mass flux using for different values of the accommodation coefficient for (a) KTG and (b) NET. In both cases $\Delta T = 10$ K.

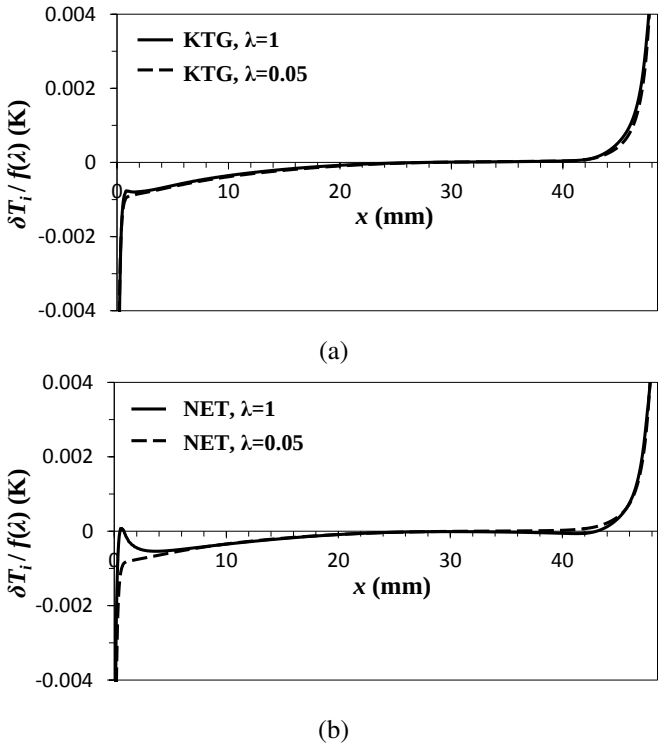

Figure 12: Scaled interfacial temperature profiles for (a) KTG and (b) NET. In both cases $\Delta T = 10$ K.

in the absence of air. In both cases, the interfacial temperature was found to be determined by the saturation temperature, with a small deviation (of order 10^{-3} K) due to the latent heat released/absorbed at the interface as a result of phase change. When the gas phase is dominated by air, the gradient in the saturation temperature is comparable to the imposed temperature gradient, and the flow is primarily driven by thermocapillary stresses. When the air is completely removed, thermocapillarity becomes negligible and the flow is driven primarily by buoyancy.

We have also investigated three different theoretical models of phase change derived using Kinetic Theory of Gases, Statistical Rate Theory, and Nonequilibrium Thermodynamics and found that their predictions are in good quantitative agreement, at least when the accommodation coefficient is set to unity. Furthermore, KTG and NET were also found to agree for other values of the accommodation coefficient. While, both SRT and NET predict a temperature jump across the liquid-vapor interface, unlike KTG, neither this temperature jump nor the dependence of the interfacial temperature on the accommodation coefficient were sufficient to explain the discrepancy between the numerical predictions and the experimental observations. The only remaining reasonable explanation is that the discrepancy between the numerical and experimental studies is the presence of a minute amount of air (molar fractions as low as a few percent) in the experimental system. The effect of residual noncondensables on the heat and mass transport in confined and sealed two-phase flows of volatile fluids, which fully confirms this hypothesis, will be discussed in a subsequent publication.

Finally, this work shows, surprisingly, that Newton's Law of Cooling, which completely breaks down at atmospheric conditions, appears to be reasonably accurate in the absence of noncondensables. Although the inapplicability of Newton's Law was admittedly demonstrated for a volatile fluid, there is no reason to expect the result to be any different for non-volatile fluids, since volatility plays a minor role when the gas phase is dominated by noncondensables. Given that a large number of one-sided transport models are based on this empirical law, the accuracy of such models at atmospheric conditions needs re-evaluation.

Acknowledgements

This work was supported by the Thermal Management Program of the Office of Naval Research under award N00014-09-1-0298. We are grateful to Hrvoje Jasak for help with numerical implementation of the model using OpenFOAM and to Minami Yoda for many useful discussions and help with preparing this manuscript.

References

[1] A. Faghri, Heat Pipe Science And Technology, Taylor & Francis Group, Boca Raton, 1995.

[2] Y. Li, R. O. Grigoriev, M. Yoda, Experimental study of the effect of noncondensables on buoyancy-thermocapillary convection in a volatile silicone oil, Phys. Fluids (2013) under consideration.

[3] T. Qin, Željko Tuković, R. O. Grigoriev, Buoyancy-thermocapillary convection of volatile fluids under atmospheric conditions, Int. J Heat Mass Transf. (2014) accepted for publication.

[4] D. Villers, J. K. Platten, Coupled buoyancy and Marangoni convection in acetone: experiments and comparison with numerical simulations, J. Fluid Mech. 234 (1992) 487–510.
[5] C. De Saedeleer, A. Garcimartín, G. Chavepeyer, J. K. Platten, G. Lebon, The instability of a liquid layer heated from the side when the upper surface is open to air, Phys. Fluids 8 (3) (1996) 670–676.
[6] A. Garcimartín, N. Mukolobwiez, F. Daviaud, Origin of waves in surface-tension-driven convection, Phys. Rev. E 56 (2) (1997) 1699–1705.
[7] R. J. Riley, G. P. Neitzel, Instability of thermocapillarybuoyancy convection in shallow layers. Part 1. Characterization of steady and oscillatory instabilities, J. Fluid Mech. 359 (1998) 143–164.
[8] H. Ben Hadid, B. Roux, Buoyancy- and thermocapillary-driven flows in differentially heated cavities for low-Prandtl-number fluids, J. Fluid Mech. 235 (1992) 1–36.
[9] M. Mundrane, A. Zebib, Oscillatory buoyant thermocapillary flow, Phys. Fluids 6 (10) (1994) 3294–3306.
[10] X. Lu, L. Zhuang, Numerical study of buoyancy- and thermocapillary-driven flows in a cavity, Acta Mech Sinica (English Series) 14 (2) (1998) 130–138.
[11] V. M. Shevtsova, A. A. Nepomnyashchy, J. C. Legros, Thermocapillary-buoyancy convection in a shallow cavity heated from the side, Phys. Rev. E 67.
[12] J. Zhang, S. J. Watson, H. Wong, Fluid Flow and Heat Transfer in a Dual-Wet Micro Heat Pipe, J. Fluid Mech. 589 (2007) 1–31.
[13] G. V. Kuznetzov, A. E. Sitnikov, Numerical Modeling of Heat and Mass Transfer in a Low-Temperature Heat Pipe, Journal of Engineering Physics and Thermophysics 75 (2002) 840–848.
[14] T. Kaya, J. Goldak, Three-Dimensional Numerical Analysis of Heat and Mass Transfer in Heat Pipes, Heat Mass Transfer 43 (2007) 775–785.
[15] K. Kafeel, A. Turan, Axi-symmetric Simulation of a Two Phase Vertical Thermosyphon using Eulerian Two-Fluid Methodology, Heat Mass Transfer 49 (2013) 1089–1099.
[16] B. Fadhl, L. C. Wrobel, H. Jouhara, Numerical Modelling of the Temperature Distribution in a Two-Phase Closed Thermosyphon, Applied Thermal Engineering 60 (2013) 122–131.
[17] J. P. Burelbach, S. G. Bankoff, S. H. Davis, Nonlinear stability of evaporating/condensing liquid films, J. Fluid Mech. 195 (1988) 463–494.
[18] R. W. Schrage, A Theoretical Study of Interface Mass Transfer, Columbia University Press, New York, 1953.
[19] P. J. Wayner, Y. K. Kao, L. V. LaCroix, The Interline heat transfer coefficient of an evaporating wetting film, Int. J. Heat Mass Transfer 19 (1976) 487–492.
[20] S. Kjelstrup, D. Bedeaux, Non-Equilibrium Thermodynamics of Heterogeneous Systems, World Scientific, Singapore, 2008.
[21] H. Struchtrup, S. Kjelstrup, D. Bedeaux, Temperature-difference-driven mass transfer through the vapor from a cold to a warm liquid, Phy. Rev. E 85 (2012) 061201.
[22] C. A. Ward, R. D. Findlay, M. Rizk, Statistical rate theory of interfacial transport. I. Theoretical development, J. Chem. Phys. 76 (1982) 5599.
[23] `http://www.openfoam.com`, 2012.
[24] R. V. Birikh, Thermocapillary convection in a horizontal layer of liquid, J. Appl. Mech. Tech. Phys. 7 (1966) 43–44.
[25] A. G. Kirdyashkin, Thermogravitational and thermocapillary flows in a horizontal liquid layer under the conditions of a horizontal temperature gradient, Int. J. Heat Mass Transfer 27 (1984) 1205–1218.
[26] D. Villers, J. K. Platten, Separation of Marangoni convection from gravitational convection in earth experiments, Phys. Chem. Hydrodyn. 8 (1987) 173–183.
[27] T. Qin, R. O. Grigoriev, Convection, evaporation, and condensation of simple and binary fluids in confined geometries, in: Proc. of the 3rd Micro/Nanoscale Heat & Mass Transfer International Conference, paper MNHMT2012–75266, 2012.
[28] C. A. Ward, D. Stanga, Interfacial conditions during evaporation or condensation of water, Phys. Rev. E 64 (2001) 051509.
[29] V. K. Badam, V. Kumar, F. Durst, K. Danov, Experimental and theoretical investigations on interfacial temperature jumps during evaporation, Exp. Therm. and Fluid Sci. 32 (2007) 276–292.
[30] F. Duan, C. A. Ward, V. K. Badam, F. Durst, Role of molecular phonons and interfacial-temperature discontinuities in water evaporation, Phys. Rev. E 78 (2008) 041130.
[31] B. Paul, Complication of evaporation coefficients, ARS J 32 (1962) 13211328.
[32] R. Marek, J. Straub, Analysis of the evaporation coefficient and the condensation coefficient of water, Int. J Heat Mass. Transf. 44 (2001) 3953.